Japanese Journal of Applied Physics
Vol. 45, No. 6A, 2006, pp. 5254–5262

Phase Tomography by X-ray Talbot Interferometry for Biological Imaging

Atsushi MOMOSE*, Wataru YASHIRO, Yoshihiro TAKEDA[1], Yoshio SUZUKI[2] and Tadashi HATTORI[3]

Department of Advanced Materials Science, School of Frontier Sciences, The University of Tokyo, 5-1-5 Kashiwanoha, Kashiwa, Chiba 277-8561, Japan
[1]*Graduate School of Pure and Applied Sciences, University of Tsukuba, 1-1-1 Tennodai, Tsukuba, Ibaraki 305-8573, Japan*
[2]*Japan Synchrotron Radiation Research Institute, 1-1-1 Kouto, Sayo, Hyogo 679-5198, Japan*
[3]*Laboratory of Advanced Science and Technology for Industry, University of Hyogo, 3-1-2 Kouto, Kamigori, Hyogo 678-1205, Japan*

(Received December 13, 2005; accepted March 5, 2006; published online June 8, 2006)

The X-ray phase tomography of biological samples is reported, which is based on X-ray Talbot interferometry. Its imaging principle is described in detail, and imaging results obtained for a cancerous rabbit liver and a mouse tail with synchrotron radiation are presented. Because an amplitude grating is needed to construct an X-ray Talbot interferometer, a high-aspect-ratio grating pattern was fabricated by X-ray lithography and gold electroplating. X-ray Talbot interferometry has an advantage that it functions with polychromatic cone-beam X-rays. Finally, the compatibility with a compact X-ray source is discussed. [DOI: 10.1143/JJAP.45.5254]

KEYWORDS: phase contrast, tomography, interferometry, Talbot effect, grating, cone beam

1. Introduction

The high sensitivity achieved by X-ray phase imaging methods has been attracting increasing attention.[1,2] Because conventional X-ray imaging methods rely on absorption in an object to be inspected, weak absorbing structures, such as biological soft tissues, cannot be imaged with a sufficient signal-to-noise ratio under the allowable X-ray dosage limit. The use of X-ray phase contrast provides a way to overcome this difficulty. This is because the interaction cross section of X-ray phase shift is about a thousand times larger than that of absorption for soft tissues.[3]

Several methods have been developed for X-ray phase imaging to date, which are categorized into the interferometric method,[4–7] refraction-based method,[8–11] and propagation-based method.[12–14] Besides the methods that only generate phase contrasts, phase measurement methods are also developed, enabling quantitative image analyses, such as phase tomography.[6,7,15–19]

X-ray phase imaging is very attractive from a clinical point of view because the sensitivity to soft tissues is tremendously increased and/or X-ray dose is considerably reduced, as compared with the conventional X-ray imaging methods. Nevertheless, the introduction of these methods to medical diagnosis is very slow. This is because X-ray sources with a quality much higher than that of conventional laboratory (or hospital) X-ray sources are required in most X-ray phase imaging methods.

As for methods using a crystal interferometer[4–7] or analyzer crystal for selecting refracted X-rays,[8–11,16–19] a restriction emerges from the fact that crystal optical elements are used. The crystal optics functions under the Bragg diffraction condition; therefore, a monochromatic and parallel beam is needed with a sufficient flux. As a result, synchrotron radiation is a sole choice available for those methods with practical imaging exposure time.

The propagation-based method[12–15] relies on the detection of Fresnel diffraction, by which an outline contrast is generated at the surface and structural boundaries of a sample. The width of the outline contrast is approximately $\sqrt{\lambda\ell}$, where λ and ℓ are the X-ray wavelength and distance between the sample and detecting plane, respectively. To resolve the outline contrast, whose width is of the order of microns even when an image is detected 1 m downstream from the sample, an image detector with an effective pixel size of the order of microns or smaller is needed. Because X-rays enough to ensure a sufficient signal-to-noise ratio are needed in a pixel, a brilliant X-ray source is required consequently. Many experiments are therefore performed at synchrotron facilities. The contribution of the outline contrast can be observed using a detector of a pixel size larger than the above estimation, and a medical apparatus has been developed on the basis of this usage for use in hospitals.[20] However, for quantitative phase measurement and thereby phase tomography, Fresnel diffraction must be observed with a sufficient spatial resolution and a sufficient signal-to-noise ratio, which are attained by synchrotron radiation.[15]

Recently, X-ray differential interferometry that employs transmission gratings has been studied for X-ray phase imaging,[21–25] which is potentially compatible with compact X-ray sources. X-ray Talbot interferometry (XTI)[22] shown in Fig. 1 is an X-ray differential interferometer consisting of a phase grating (G1) and an amplitude grating (G2). XTI may provide an opportunity for the instrumentation outside synchrotron facilities, because it functions in principle with a cone beam with a broad energy band width.

The principle of XTI is the same as that of optical Talbot interferometry,[26,27] but the fabrication of an amplitude

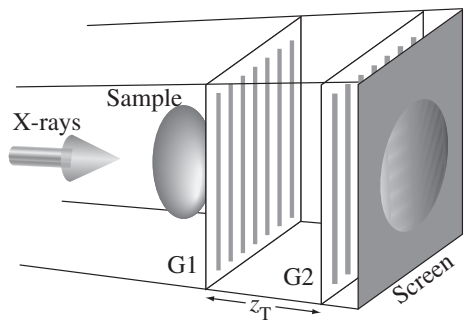

Fig. 1. Configuration of XTI, where two transmission gratings (G1 and G2) are arranged in line along X-ray axis.

*E-mail address: momose@exp.t.u-tokyo.ac.jp

X-ray grating is a difficulty that needs to be overcome to realize XTI. Because of the high penetrating power of X-rays, a thick pattern must be fabricated to block X-rays fully. At the same time, the period of the grating should be of the order of microns, as explained later according to the principle of XTI. The fabrication of a pattern with such a high aspect ratio is not straightforward.

A capillary plate, which has a two-dimensional array of holes in a lead glass plate with an aspect ratio that meets already the requirement for XTI, is a candidate device for the amplitude X-ray grating.[28] However, its quality, such as the uniformity of the pitch of the hole array, is currently unsatisfactory. A line and space (L&S) pattern is used for a simple and typical grating and available for XTI. However, the fabrication of a high-aspect-ratio L&S pattern is difficult using conventional lithographic techniques. However, X-ray lithography is attractive for that purpose, and in this study we used a grating fabricated by X-ray lithography and electroplating of gold,[29] which was selected as a material for blocking X-rays because of its high absorption coefficient and technical convenience in the fabrication process.

In this paper, theoretical aspects of XTI are described first, including the procedure of phase tomography. Then, we report evaluation results of an X-ray Talbot interferometer constructed with gold gratings. We performed phase tomography measurements on biological soft tissues with the interferometer using synchrotron radiation, and reconstructed images are presented next. Finally, future prospects of XTI are discussed.

2. X-ray Talbot Interferometry

2.1 Principle of phase imaging

The principle of XTI was described in a previous paper[22] but again described here, adding more details, for the following explanation of phase tomography based on XTI.

The function of XTI is based on the X-ray (fractional) Talbot effect[30] discovered originally in the visible light region,[31] which is known as a self-imaging effect by an object with a periodic structure under coherent illumination. While a transmission image becomes blurry with increasing distance from an object to an imaging plane under normal illumination, self-images are reconstructed at specific distances from a periodic object to an imaging plane by the Talbot effect. This phenomenon is understood as a result of Fresnel or Fraunhofer diffraction.

Let us consider a situation in which a grating of a period d is illuminated coherently with unit-amplitude plane-wave X-rays of wavelength λ. Given the complex transmission function $T(x, y)$ of the grating with a Fourier expansion series

$$T(x, y) = \sum_n \alpha_n \exp\left(2\pi i \frac{nx}{d}\right), \tag{1}$$

the wave field $E(x, y, z)$ behind the grating is written as

$$E(x, y, z) = \sum_n \beta_n(z) \exp\left(2\pi i \frac{nx}{d}\right) \tag{2}$$

under a paraxial approximation, where

$$\beta_n(z) \equiv \alpha_n \exp(-\pi i \lambda z n^2/d^2). \tag{3}$$

Here, the optical axis is parallel to the z axis, and the grating is on the (x, y) plane ($z = 0$) and has periodicity in the x direction. Equations (2) and (3) imply that the periodic pattern in the wave field varies and oscillates as induced by propagation. The intensity of the wave field is given by

$$I_s(x, y, z) = |E(x, y, z)|^2 = \sum_n a_n(z) \exp\left(2\pi i \frac{nx}{d}\right), \tag{4}$$

where

$$a_n(z) \equiv \sum_{n'} \beta_{n+n'} \beta^*_{n'}. \tag{5}$$

The distances z_T given by

$$z_T = md^2/\lambda, \tag{6}$$

where m is an integer for an amplitude grating or a half integer for a phase grating, are particularly interesting. If m is an even integer, $\beta_n(z_T) = \alpha_n$; therefore, a wave field whose complex amplitude is the same as the complex transmission function of the grating is generated (Talbot effect). If m is an odd integer, $\beta_n(z_T) = -\alpha_n$, and a wave field with a complex amplitude of $T(x + d/2)$ is generated (a case of fractional Talbot effect); that is, the contrast is inverted. When a phase grating is used, no intensity patterns are observed at the distances. However, if m is a half integer, the phase modulation pattern $T(x) = \exp[i\phi(x)]$ is converted into intensity patterns, which are also called self-images in this work, as given by

$$|E(x, y, z_T)|^2 = 1 \pm \sin\{\phi(x) - \phi(x + d/2)\}, \tag{7}$$

where $\pm$ corresponds to cases in which $m - 1/2$ is even and odd.[32] Visibility is therefore at the maximum when the magnitude of phase modulation is $\pi/2$ while a π phase grating is used in many applications because $\pm$1st-order diffractions are enhanced, suppressing the 0th order. The self-image of a $\pi/2$ phase grating is understood as a constructive superposition of interference fringes mainly between neighboring orders (i.e., 0th and $\pm$1st orders, $\pm$1st and $\pm$2nd orders, ...).

Under partial coherent illumination, the visibility of a self-image is degraded and its influence can be reflected in eq. (4) by replacing $a_n(z)$ with $\mu(n\lambda z/d)a_n(z)$, where μ is the complex degree of coherence, which is given by the Fourier transform of the distribution of an X-ray source, according to the van Cittert–Zernike theorem.[33]

Next, let us consider a case in which the incident X-ray wave is deformed due to the phase shift $\Phi(x, y)$ caused by an object placed in front of the grating. In this case, the self-image is also deformed as illustrated in Fig. 2 and its intensity is given by

$$I_s(x, y, z) = \sum_n a'_n(x, y, z) \exp\left[2\pi i \frac{n}{d}(x - z\varphi_x(x, y))\right], \tag{8}$$

where

$$\varphi_x(x, y) = \frac{\lambda}{2\pi} \frac{\partial \Phi(x, y)}{\partial x} \tag{9}$$

and $a_n(z)$ has been replaced with $a'_n(x, y, z)$, which takes into consideration the effect of X-ray attenuation by the sample. The amount of deformation is proportional to z.

It is therefore possible to detect the object by analyzing the deformed self-image by using an image detector with

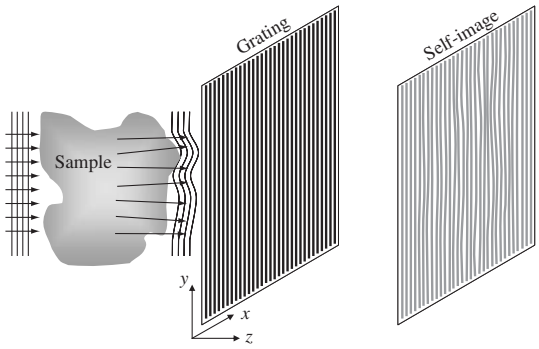

Fig. 2. Deformation of self-image by refraction at sample placed in front of grating.

a spatial resolution below d (of the order of microns). However, an X-ray image detector with such a resolution is rare. Instead XTI uses another grating at the position of the self-image, as illustrated in Fig. 1. If the period of the second grating is almost the same as that of the self-image, a moiré fringe pattern is generated by the superposition of the deformed self-image and the pattern of the second grating. The deformation of the self-image is also reflected on the moiré pattern. Because a typical fringe spacing is much larger than d, normal X-ray image detectors are available.

Giving the transmission function $t(x,y)$ of the second grating with a Fourier expansion series as

$$t(x,y) = \sum_n b_n \exp\left(2\pi i \frac{nx}{d}\right), \tag{10}$$

a moiré pattern is given by

$$\begin{aligned} I(x,y,z) &= I_s(x,y,z) \times t(x,y) \\ &= \sum_n a'_n(x,y,z) b_{\bar{n}} \exp\left\{2\pi i \frac{n}{d}\left(y\theta + z\varphi_x(x,y) + \chi\right)\right\}, \end{aligned} \tag{11}$$

where θ ($\ll 1$) and χ are the relative inclination and displacement, respectively, in the (x,y) plane of the second grating against the first. The factor describing the contrast with the period of d has been averaged out.

2.2 Phase tomography

The X-ray phase shift $\Phi(x,y)$ is written as

$$\Phi(x,y) = \frac{2\pi}{\lambda}\int \delta(x,y,z)\,dz, \tag{12}$$

where $\delta(x,y,z)$ is the refractive index decrement from unity. Therefore, if phase shifts are measured in plural projection directions, $\delta(x,y,z)$ is reconstructed with the algorithm of computed tomography. This is X-ray phase tomography.[6] The quantitative measurement of $\Phi(x,y)$ is therefore significant. In the case of XTI, φ_x is determined from moiré patterns. Then, Φ is obtained by integration, enabling X-ray phase tomography.

To determine φ_x from the moiré patterns, phase-shifting interferometry (or fringe-scanning method)[34] is available. Normal phase-shifting interferometry assumes a two-beam interference, which generates a sinusoidal fringe profile in general given by $A + B\cos\Phi$, where A and B are the average intensity and fringe contrast. By introducing a phase difference that varies with a step of $2\pi/M$ (M: integer), interference patterns

$$I^{(k)}(x,y) = A(x,y) + B(x,y)\cos\left\{\Phi(x,y) + \frac{2\pi k}{M}\right\} \quad (k = 1,2,\ldots,M) \tag{13}$$

are measured, and Φ is calculated using

$$\Phi(x,y) = \arg\left[\sum_{k=1}^{M} I^{(k)}(x,y)\exp\left(-2\pi i\frac{k}{M}\right)\right]. \tag{14}$$

In the case of XTI that causes multibeam differential interference, by changing χ in eq. (11) with a step of d/M (M: integer), moiré patterns

$$\begin{aligned} I^{(k)}(x,y,z_{\mathrm{T}}) &= \sum_n a'_n(x,y,z_{\mathrm{T}}) b_{\bar{n}} \\ &\times \exp\left\{2\pi i\frac{n}{d}\left(y\theta + z_{\mathrm{T}}\varphi_x(x,y) + \frac{kd}{M}\right)\right\} \end{aligned} \tag{15}$$

are measured. If the 0th and $\pm$1st orders are dominant, it is clear that the operation of eq. (14) is available; that is,

$$\begin{aligned} &\frac{2\pi}{d}(y\theta + z_{\mathrm{T}}\varphi_x(x,y)) \\ &= \arg\left[\sum_{k=1}^{M} I^{(k)}(x,y,z_{\mathrm{T}})\exp\left(-2\pi i\frac{k}{M}\right)\right]. \end{aligned} \tag{16}$$

The influence of higher orders is considered as below. The substitution of eq. (15) into the right hand side of eq. (16) yields

$$\begin{aligned} &\arg\left[\sum_n a'_n(x,y,z_{\mathrm{T}}) b_{\bar{n}} C_{n,M}\right. \\ &\left.\times \exp\left\{i2\pi\frac{n}{d}(y\theta + z_{\mathrm{T}}\varphi_x(x,y))\right\}\right], \end{aligned} \tag{17}$$

where

$$\begin{aligned} C_{n,M} &\equiv \sum_{k=1}^{M}\exp\left\{2\pi i\frac{k}{M}(n-1)\right\} \\ &= \begin{cases} M & \text{if } n-1 = qM \\ 0 & \text{otherwise} \end{cases} \quad q\text{: integer.} \end{aligned} \tag{18}$$

The combinations of n and M that yield non-zero values of $C_{n,M}$ are shown in Table I, which suggests that if a sufficiently large number is selected for M, the influence of higher orders is cancelled out and eq. (16) is available.[35]

Here, it should be noted that even orders can be ignored if the gratings have 1:1 L&S patterns. Then, when $M = 5$, the lowest order is ninth, which causes an error in calculating φ_x using eq. (16). The magnitude of such a high order is very small normally. In addition, actual grating patterns are not

Table I. Combinations of n and M indicated by "e" yield non-zero values of $C_{n,M}$ and cause errors in calculating φ_x using eq. (16).

M	Harmonics ($\lvert n\rvert$)							
	2	3	4	5	6	7	8	9
3	e	—	e	e	—	e	e	—
4	—	e	—	e	—	e	—	e
5	—	—	e	—	e	—	—	e
6	—	—	—	e	—	e	—	—
7	—	—	—	—	e	—	e	—
8	—	—	—	—	—	e	—	e

completely rectangular and the spatial coherency of X-rays that impinge on the gratings is normally incomplete. These factors decrease higher orders and contribute to reducing errors in calculating φ_x using eq. (16). Thus, $M = 5$ is a kind of magic number suitable for applying the technique of phase-shifting interferometry to XTI. The absorption contrast caused by the sample, which is involved in a'_n, is eliminated by this procedure, and the resultant image maps purely the differential phase shift φ_x.

Normally, φ_x is determined by measurements with and without a sample. Then, the effect of θ on eq. (16) is removed by subtraction. In addition, the effect of the imperfection of gratings and/or deformed wavefronts of incident X-rays are excluded as well.

The right term of eq. (16) involves the operation of arctangent, whose value ranges from $-\pi$ to π. Therefore, when X-rays are refracted partially exceeding the amount corresponding to the range, jumps between $-\pi$ and π are found in the resultant image obtained by the calculation of eq. (16). In such a case, we need a process for *unwrapping* the jumps by adding (subtracting) 2π to (from) one of the pixels neighboring across the jumps. When the jump lines are clear, the procedure is completed without errors. However, the jump lines become unclear occasionally when the data is noisy or when regions of steep value changes are contained. Sophisticated techniques are developed to enable unwrapping in such cases, and we used a cut-line algorithm[36] in the present study.

Finally, Φ is obtained by calculating

$$\Phi(x, y) = \frac{2\pi}{\lambda} \int \varphi_x(x, y)\, dx + C, \tag{19}$$

and the constant of integration C is determined by the fact that a sample is surrounded by a null region in the measurement by tomography; that is, $C = 0$. By repeating this measurement at various angular positions of the sample rotation, one can reconstruct $\delta(x, y, z)$ using a conventional algorithm in computed tomography.

One can skip this integration process if an algorithm with a filter function for beam-deflection optical tomography[37] is used; in the case of the convolution-backprojection method,

$$H(h\Delta x) = \begin{cases} \dfrac{1}{\pi^2 h \Delta x} & h\text{: odd} \\ 0 & h\text{: even} \end{cases} \tag{20}$$

is the filter function to be used, where Δx is the pixel size.

As a summary of this section, images at each image processing step described above are shown in Fig. 3 using the data of the phantom experiment reported previously.[23]

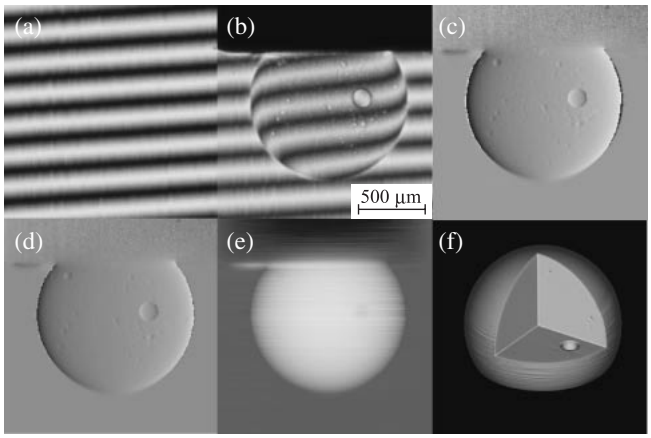

Fig. 3. Images at each step of phase tomography with XTI. A moiré pattern (a), which was due to the relative inclination (θ) of the grating against the other, is deformed by the differential phase shift caused by a sample (plastic sphere about 1 mm in diameter with some air bubbles in it) placed in the field of view, as shown in (b). (c) was obtained by a five-step fringe scan. The effect of θ was removed using (a). Because (c) is the output of eq. (16), the image is *wrapped*, and after an unwrapping procedure, (d) that exhibits φ_x is obtained. Black-white jumps observed in the outline region of the sphere in (c) are compensated. (e), which is to be input to the reconstruction algorithm of tomography, is obtained through the spatial integration of (d). Repeating this series of procedure at every angular position of the sample rotation, a three-dimensional image (f) mapping the refractive index is reconstructed, where one quadrant has been cropped to show the inside.

3. Experiments

3.1 Grating

We selected gold as a material for the grating pattern because its absorption coefficient is comparatively large. Nevertheless, the thickness should be much more than ten microns. As for the grating period, it should be smaller than or comparable to the X-ray spatial coherence length, which is several microns typically, and as a result a pattern of a high aspect ratio must be fabricated.

Although microfabrication by optical lithography is routinely performed, it is difficult to form a L&S pattern whose thickness exceeds ten microns. A solution is found in the field of X-ray lithography, which enables the formation of a high-aspect-ratio structure, taking advantage of the property of X-rays, that is, they tend to go straight in comparison with light of longer wavelengths. In this study, we used an X-ray amplitude grating fabricated by X-ray lithography and gold electroplating, as described below.

The synchrotron radiation beamline 11 of NewSUBARU, Japan, which is dedicated to Lithographie Galvanoformung Abformung (LIGA) fabrication, was used. A 30 μm X-ray resist film (MAX001, Nagase ChemteX) was spin-coated on a 200-μm Si wafer with a 0.25-μm Ti layer, and then a 4-μm L&S resist pattern ($d = 8$ μm) was fabricated by X-ray exposure. Gold lines were formed by electroplating between resist lines, which were left after the electroplating to support the gold lines (Fig. 4). The effect of absorption by the X-ray resist is negligible. The height of the gold lines

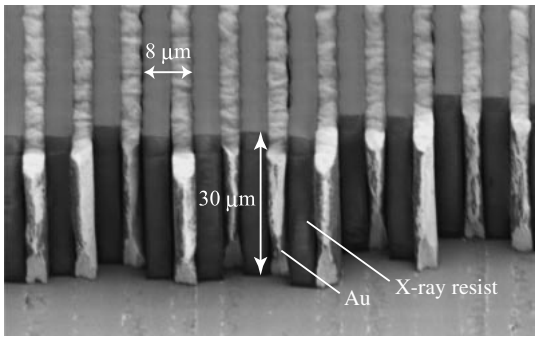

Fig. 4. SEM image of X-ray amplitude grating fabricated by X-ray lithography and gold electroplating. This grating was used for the second grating in XTI.

was nearly 30 μm, and the effective area of the grating was $20 \times 20\,\mathrm{mm}^2$.[29]

The first grating was also fabricated in a similar manner, except that UV lithography was used, and had a gold pattern, which was much thinner than that of the second. The thickness was experimentally evaluated to be optimal for X-rays of about 0.065 nm for a $\pi/2$ phase grating. An amplitude grating is available for the first grating, but a phase grating is superior to an amplitude grating in that X-ray intensity is twice at an image detector and that the requirement for spatial coherency is moderated because z_T is reduced by one-half.

3.2 *Performance of XTI*

An X-ray Talbot interferometer was arranged at the beamline 20XU of SPring-8, Japan, where undulator X-rays were available at 245 m from the source point. The vertical source size of synchrotron radiation is normally much smaller than the horizontal size. However, because the effect of the instability of the beamline monochromator existed, the gratings were aligned so that the gold pattern was almost vertical. Then, spatial coherency was determined by horizontal source size. Strictly, in the present case, source size was determined by the front-end slit 400 μm in width located 214 m upstream from the grating. The spatial coherence was certainly larger than d (= 8 μm).

Figure 5 shows moiré patterns observed with 0.065-nm X-rays with the visibility as a function of the distance between the gratings. Here, θ was 1.3° and therefore the moiré fringes were generated. Although this study was performed assuming that synchrotron radiation is a plane wave, strictly a spherical wave with a small curvature was introduced into the interferometer, and its effect was observed as the inclination of fringes; that is, the horizontal component of spatial frequency is due to the mismatch of the period between the second grating and the self-image of the first grating, which was enlarged by slightly spherical-wave illumination.

At $z = d^2/2\lambda$, which was the best position for XTI with a $\pi/2$ phase grating, the fringe visibility exceeded 0.8. With increasing the distance, visibility minimized at $z \approx d^2/\lambda$ and again increased, indicating that this phenomenon was induced by the fractional Talbot effect. Strictly, a minimum was found at a distance slightly shorter than d^2/λ. This is considered to be due to the coexisting amplitude modulation caused by the first grating.

The influence of higher orders when using eq. (16) was commented above. Figure 6 shows the Fourier-transforms of the moiré patterns shown in Fig. 5. In Fig. 6(b), that is, the

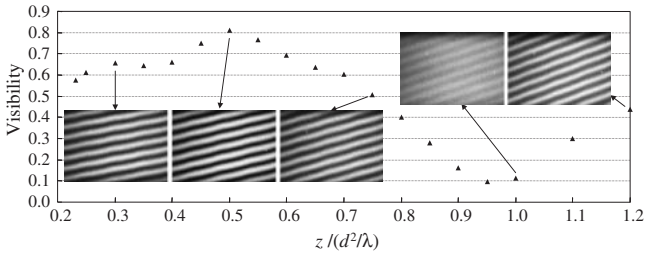

Fig. 5. Moiré patterns and their visibilities observed by XTI at various spacings between two gratings. $\lambda = 0.065$ nm.

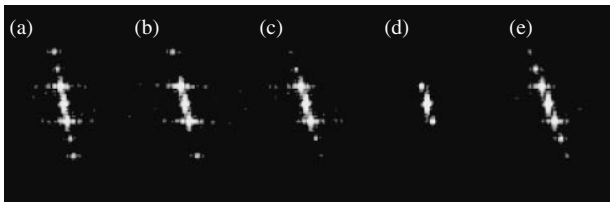

Fig. 6. Fourier-transforms of moiré patterns shown in Fig. 5 in the same order.

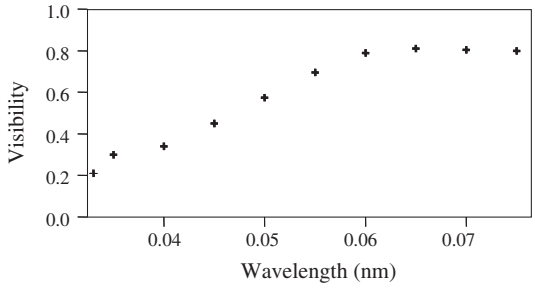

Fig. 7. Visibility of moiré pattern as function of X-ray wavelength. The distance between gratings was kept at $d^2/2\lambda$.

Fourier transform of the moiré pattern of the best visibility, spots of 0th, 1st, and 3rd orders existed, and those of higher orders and even orders were not detected. This result confirmed that the selection of 5 for M as discussed above was reasonable for the experiments of phase tomography that will be presented below. However, at the same time, it was found that other Fourier-transforms exhibited even orders as shown in Fig. 6. Therefore, one should be careful when XTI is operated with the grating separation widely different from $d^2/2\lambda$ even if the visibility is still high.

Next, keeping the condition $z = d^2/2\lambda$, the visibility was plotted as a function of λ (Fig. 7). This result shows that the Talbot interferometer functioned in a wide energy range; the visibility was over 0.3 even at 0.04 nm (31 keV). The availability of the interferometer at higher energy is meaningful because the observation of high-density tissues such as bone and calcification becomes more feasible, revealing soft tissue structures in the same view.

3.3 *Phase tomography of biological samples*

The X-ray Talbot interferometer was used for the tomographic observation of biological soft tissues. A sample was fixed on the tip of a rotation rod and immersed in formalin filling a cell. Because of the problem of bubble generation in the cell due to intense X-ray irradiation, beam intensity was moderately reduced by undulator-gap detuning. The flux density at a sample was approximately 10^{11} photons $\mathrm{mm}^{-2}\,\mathrm{s}^{-1}$.

The measurement of $\varphi_x(x, y)$ by a five-step fringe scan was repeated at each angular position of the sample rotation with a step of 0.72° over 180°. Images were recorded using a CCD camera coupled with optical lens and a phosphor screen, whose effective pixel size was 4.34 μm. The tomograms presented below are therefore formed by voxels 4.34 μm on one side. Exposure times for recording a moiré pattern were 1.0, 0.2, and 0.25 s for Figs. 8, 9, and 10, respectively.

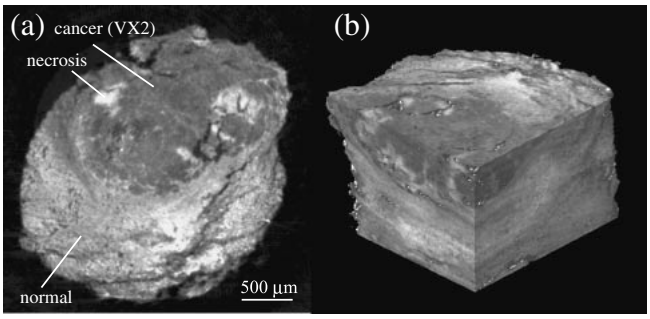

Fig. 8. Rabbit liver tissue with VX2 cancer examined by phase tomography with 0.1 nm X-rays. Cancerous lesion was clearly differentiated from normal tissue in (a), and necrosis in the tumor was revealed. (b) is a three-dimensional rendering view of a part of reconstructed data.

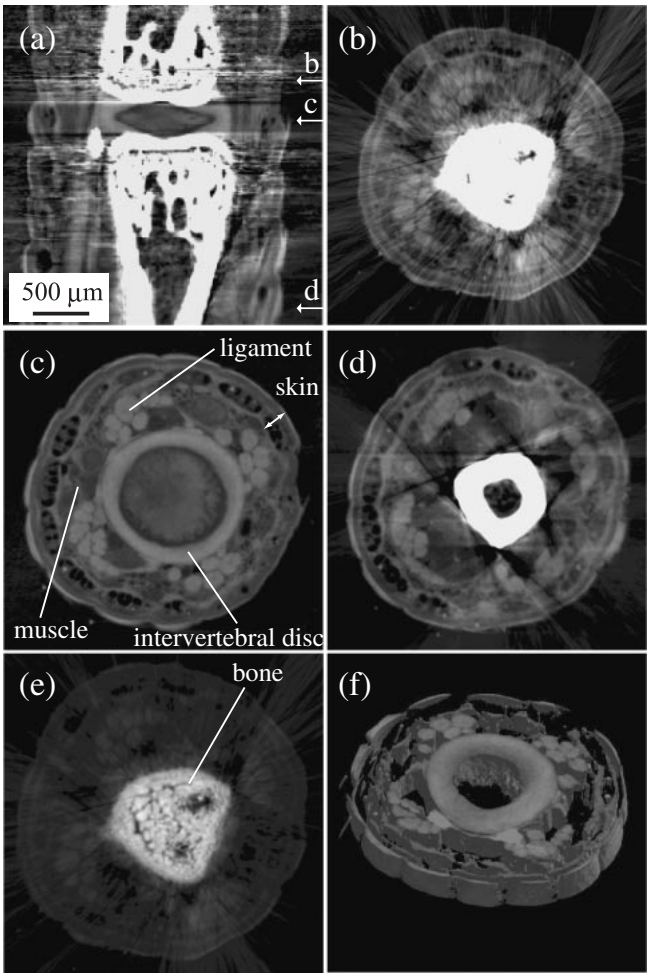

Fig. 9. Mouse tail observed by phase tomography with 0.07 nm X-rays. In the sagital image (a), the positions of the axial images (b), (c), and (d) are indicated by arrows. The grayscale of (b)–(d) corresponds to the refractive index difference ranging from 0 to 2×10^{-7}. A redrawing of (b) with a grayscale from 0 to 7×10^{-7} is shown in (e), where a trabecular structure of the bone is shown. (f) is a three-dimensional rendering view of a portion containing an intervertebral disc.

A piece of rabbit liver with cancer (VX2) was first examined using 0.1 nm X-rays. A cancerous lesion depicted with a lower grayscale value was clearly differentiated from a normal tissue as shown in Fig. 8. Furthermore, necrosis was detected as bright areas in the cancerous lesion. The grayscale corresponds to the refractive index difference

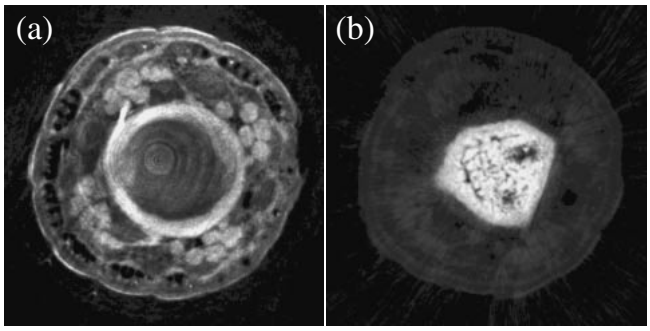

Fig. 10. Mouse tail identical to sample shown in Fig. 9, observed by phase tomography with 0.04 nm X-rays. The slice positions of (a) and (b) correspond to those of Figs. 9(c) and 9(e). The grayscales of (a) and (b) correspond to the refractive index difference ranging from 0 to 6×10^{-8} and to 2×10^{-7}, respectively.

ranging from 0 to 1.1×10^{-7}. This feature is comparable to the result obtained by phase tomography using a Mach–Zehnder type crystal X-ray interferometer.[38)]

XTI is available for a sample containing bone tissue, while phase tomography with a crystal X-ray interferometer is not suitable for such a sample because interference fringes that are too fine to resolve are generated by bones. Figure 9 shows a result obtained for a mouse tail using 0.07 nm X-rays. The arrows in the sagital image [Fig. 9(a)] indicate the positions of axial images shown in Figs. 9(b)–9(d). Soft tissue structures, such as muscle, ligament, skin, and intervertebral disc (cartilage), were depicted with bones in the same view although the bones generated some artifacts. The bones in these views are saturated, but a trabecular structure was depicted by changing the grayscale, as shown in Fig. 9(e).

It should be noted that the contrast of the bones does not include the contribution of absorption, which was eliminated by the operation in eq. (16). If the information of absorption is needed, it can be obtained by calculating amplitude instead of the argument as in the right term of eq. (16).

The X-ray Talbot interferometer functioned using 0.04 nm X-rays, as suggested by the result shown in Fig. 7. Therefore, the mouse tail was observed at this wavelength, as shown in Fig. 10, whose axial positions corresponded to those of Figs. 9(c) and 9(e). Although Fig. 10 seems to be slightly noisier than Fig. 9, one reason for which is the lower visibility of moiré fringes at 0.04 nm, this result fully suggests that our X-ray Talbot interferometer is available for X-ray phase tomography at this energy.

4. Discussion

4.1 Resolution

The spatial resolution of an image obtained by XTI is limited by the period of the grating. Including other factors such as the resolution of the image detector and noise, actual spatial resolution is determined. We evaluated spatial resolution on the basis of the average full width at half maximum (FWHM) of differential contrast profiles across boundaries between the sample and surrounding medium (formalin) in phase tomograms. From Figs. 8 and 10, 14 and 16 μm were obtained, respectively. To improve spatial resolution, gratings of a smaller period are necessary.

Contrast resolution, which describes the high sensitivity

of X-ray phase imaging, was evaluated on the basis of the standard deviation in the tomograms at the region of the surrounding formalin. In the X-ray energy region, the refractive index decrement δ, which phase tomography reveals as explained, is approximately given by

$$\delta = \frac{r_e \lambda^2}{2\pi} \rho, \tag{21}$$

where r_e is the classical electron radius and ρ is the electron density. This implies that the contrast in phase tomograms corresponds to a map of electron density. Furthermore, particularly for materials consisting of light elements, electron density is approximately proportional to mass density. Therefore, a phase tomogram is considered to be a mass density map. The standard deviation of voxel values in a part of the surrounding formalin region of Fig. 8 was 1.9×10^{-9}. The detection limit of density deviation was therefore estimated to be 1.3 mg/cm^3 because the δ of formalin, which is almost the same as that of water,[39] is 1.5×10^{-6} for 0.1 nm X-rays. Similarly, we obtained 2.2 and 5.9 mg/cm^3 for 0.07 and 0.04 nm X-rays, respectively, from Figs. 9 and 10. Thus, the sensitivity to density deviation is better with X-rays of longer wavelengths. This result is consistent with the fact that δ is proportional to the square of λ [eq. (21)].

However, it should be emphasized that errors in the unwrapping are reduced with decreasing wavelength. This is because a too strong refraction is suppressed moderately, therefore, a too rapid change in resultant φ_x is reduced. For samples containing high-density regions such as bone, the use of higher energy X-rays is significant in this sense.

4.2 Requirements for X-ray beam quality

The experiments reported in this paper were performed with synchrotron radiation assuming plane-wave monochromatic X-rays. However, as mentioned in the Introduction, XTI functions in principle with spherical-wave (cone-beam) X-rays with a broad energy band because of the use of grating optics. Here, the performance of XTI is discussed when polychromatic X-rays are used.

The change in φ_x caused by the spectral change $\Delta\lambda$ is given using eqs. (9), (12), and (21) by

$$\Delta\varphi_x = \Delta\lambda \frac{r_e \lambda}{\pi} \int \frac{\partial \rho}{\partial x} dz. \tag{22}$$

Because the positions of moiré fringes are determined by the maximum of $\cos(2\pi z_T \varphi_x / d)$, as suggested in eq. (11), the spectral change moves moiré fringes in proportion to

$$\frac{2\pi}{d} z_T \Delta\varphi_x = 2 m r_e \Delta\lambda d \int \frac{\partial \rho}{\partial x} dz. \tag{23}$$

As a result, a finite band width causes a decrease in the visibility of moiré fringes. An acceptable band width so that moiré fringes are not smeared out is evaluated using

$$2 m r_e \Delta\lambda\, d \int \frac{\partial \rho}{\partial x} dz < \frac{\pi}{2}. \tag{24}$$

Here, let us consider a case of detecting an air bubble in water. We assume that the pixel size of an image detector is d, which is the same as the period of the grating, since a smaller pixel size is meaningless because the spatial resolution of XTI is limited by d according to its principle. Then, the maximum gradient that would be measured with a discrete sampling is $\sqrt{D/d}$, where D is the diameter of the air bubble, and eq. (24) is rewritten as

$$4 m r_e \Delta\lambda\, d\rho \sqrt{\frac{D}{d}} < \frac{\pi}{2}. \tag{25}$$

Using the parameters used in this study ($d = 8\,\mu$m, $m = 1/2$) and $\rho = 3.3 \times 10^{29}\,\mathrm{m}^{-3}$ for water,

$$\Delta\lambda \sqrt{D} < 2.9 \times 10^{-13}, \tag{26}$$

where $\Delta\lambda$ and D are given with the unit of meter. This implies that $\Delta\lambda$ can be broaden up to 29 pm without smearing out an air bubble 100 µm in diameter in water. Thus, X-rays with a bandwidth $\Delta\lambda/\lambda \sim 0.1$ are certainly available. However, this result suggests at the same time that a narrower band should be selected so as to satisfy eq. (24) when a thicker object is observed.

The above discussion was presented neglecting the degradation of the performance of XTI by band width. Because z_T is inversely proportional to λ, the visibility of moiré fringes should be worse in the case of using polychromatic X-rays than in the case of using monochromatic X-rays. The contrast of the self-image has maxima along z every d^2/λ, as suggested by eq. (6). Assuming that the change in z_T induced by the spectral change of $\pm\Delta\lambda$ is smaller than $(1/4)(d^2/\bar{\lambda})$, a condition that moiré fringes are visible would be given by

$$\frac{\Delta\lambda}{\bar{\lambda}} < \frac{1}{8}, \tag{27}$$

where $\bar{\lambda}$ is the central wavelength. Thus, XTI is tolerant of the broadness of X-ray spectrum.

The above result implies that XTI does not require temporal coherency for its operation. However, requirement for spatial coherency should be noted. From the viewpoint of geometrical optics, the Talbot effect is understood as a result of interference mainly between neighboring diffraction orders generated by the grating. The angular difference between two beams of neighboring orders is λ/d, and therefore an interference fringe pattern, or self-image, with a period d is formed. Because the two beams are spatially separated by $\lambda z_T/d = md$ at $z = z_T$, the spatial coherence length should be approximately larger than md, in the case of presented study $d/2$.

In general, the spatial coherence length L is defined by

$$L = \frac{\lambda R}{2\pi\sigma_x}, \tag{28}$$

at the distance R from an X-ray source with a Gaussian intensity distribution $\exp(-x^2/2\sigma_x^2)$. Figure 11 shows the fringe visibilities of the self-image of a $\pi/2$ phase grating at $z = d^2/2\lambda$ as a function of L/d. The visibility curve is independent of λ, and when the coherence length is larger than one-half of the grating period, a self-image with a visibility of more than 0.7 is produced, which is enough for phase imaging provided the pattern of the second grating is sufficiently thick. It is noteworthy that a visibility of 0.4 is attained even $L/d \approx 1/3$.

4.3 Prospects

As presented, phase imaging at 0.04 nm was successful,

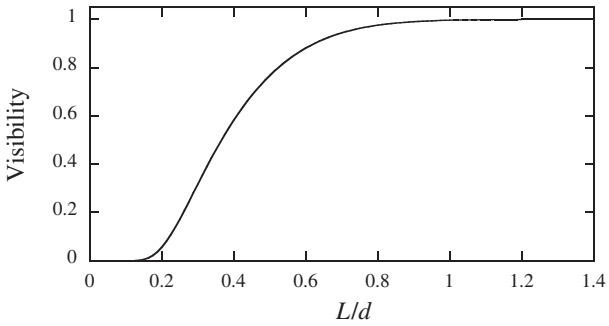

Fig. 11. Visibility of self-image of $\pi/2$ phase grating at $z = d^2/2\lambda$ as function of ratio of coherence length (L) and period of grating (d).

but it is of course necessary to fabricate a thicker pattern to attain a better imaging quality at this or a higher-energy region. At the same time, the area of the grating should be increased for practical imaging applications. The period of the gratings is also preferred to be shortened because the system can be compact and the requirement for spatial coherency is moderated. We consider that such developments are possible by improving the fabrication technology used in this study.

Although this study demonstrated XTI with synchrotron radiation, which can be assumed to be plane-wave X-rays, the development of cone-beam XTI with a compact X-ray source is significant for practical applications. The principle of XTI is common in cone-beam XTI, aside from some modifications. When a spherical wave is used, the positions of self-imaging given by eq. (6) for the plane-wave case must be replaced by

$$z_{\mathrm{T}} = \frac{md_1^2 R}{R\lambda - md_1^2}, \tag{29}$$

where R is the distance between the source and the first grating with a period d_1.[40] The period d_2 of the second grating is different from d_1 and has a relation

$$d_1 : d_2 = R : (R + z_{\mathrm{T}}). \tag{30}$$

Although the use of spherical gratings would be ideal in this case, flat gratings are also available for XTI with a spherical wave, provided that R is sufficiently larger than the size of the field of view, theoretical considerations on which will be described elsewhere.[41]

As for an image detector, XTI does not require a spatial resolution as high as that for resolving the self-image. Therefore, a variety of X-ray image detectors should be compatible with XTI. Here, it should be noted that an image detector in combination with the two gratings can be considered as a phase-sensitive image detector. In this sense, XTI is a breakthrough for the development of the first X-ray wavefront sensor.

Because XTI is operated with a cone beam with a broad energy band, its instrumentation outside synchrotron radiation facilities is highly expected. What types of X-ray source are available for cone-beam XTI? Normal X-ray generators used in hospitals are not available because of the lack of spatial coherency. The source size and source-grating distance must be selected to produce a spatial coherence length enough to generate the Talbot effect. It is therefore preferable to use a small source at a position far from it [see eq. (28)]. For instance, if $d_1 = 5\,\mu\mathrm{m}$, $\lambda = 0.04\,\mathrm{nm}$, and $\sigma_x = 5\,\mu\mathrm{m}$ (FWHM of the source size is about $12\,\mu\mathrm{m}$), then R should be larger than 2 m. At the same time, a sufficient flux is needed for imaging with a practical exposure time. These two requirements are contrary to each other.

Assuming that 10^3 photons/s are needed per $50\,\mu\mathrm{m}$ pixel for phase imaging and that a field of view of $100 \times 100\,\mathrm{mm}^2$ is covered with an array of pixels, an X-ray source emitting 2×10^{13} photons/s in the entire solid angle is required under the above conditions with respect to σ_x and R. Even taking into account the bandwidth available for XTI discussed above, the wattage of such an X-ray source should be over 100 W, which is much higher than that of commercially available microfocus X-ray generators. Although the requirement for X-ray sources is moderated using XTI as discussed above, we need to make an effort as well to develop a microfocus X-ray source with an improved brightness for practical phase imaging by XTI.

5. Conclusions

The principle of X-ray phase imaging and phase tomography with XTI was described, and successful biological imaging results with synchrotron radiation were presented. The key for the construction of an X-ray Talbot interferometer is the fabrication of an amplitude grating, because a high-aspect-ratio pattern must be formed. We fabricated a gold grating by X-ray lithography and electroplating. The X-ray Talbot interferometer with the gold grating functioned with synchrotron X-rays down to 0.04 nm wavelength. Provided that a grating with a higher aspect ratio and a wider effective area is fabricated, XTI is an attractive candidate for practical X-ray phase imaging, such as that for clinical diagnoses, because XTI has an advantage in that cone-beam X-rays of a broad energy band are available, allowing its compatibility with a compact X-ray source.

Acknowledgements

We appreciate the biological samples provided by Drs. J. Wu and T. Takeda (University of Tsukuba, Japan), the use of which was approved by the Medical Committee for the Use of Animals in Research of University of Tsukuba. The experiments using synchrotron radiation were performed under the approval of SPring-8 committee 2005A0326-NM-np. This study was financially supported by the project "Development of System and Technology for Advanced Measurement and Analysis" of Japan Science and Technology Agency (JST).

1) R. Fitzgerald: Phys. Today **53** (2000) 23.
2) A. Momose: Jpn. J. Appl. Phys. **44** (2005) 6355.
3) A. Momose and J. Fukuda: Med. Phys. **22** (1995) 375.
4) U. Bonse and M. Hart: Appl. Phys. Lett. **6** (1965) 155.
5) M. Ando and S. Hosoya: Proc. 6th Int. Conf. X-ray Optics and Microanalysis, Tokyo, 1972, p. 63.
6) A. Momose: Nucl. Instrum. Methods Phys. Res., Sect. A **352** (1995) 622.
7) F. Beckmann, U. Bonse, F. Busch and O. Günnewig: J. Comput. Assist. Tomogr. **21** (1997) 539.
8) V. A. Somenkov, A. K. Tkalich and S. Sh. Shil'shtein: Sov. Phys. Tech. Phys. **36** (1991) 1309.
9) T. J. Davis, D. Gao, T. E. Gureyev, A. W. Stevenson and S. W. Wilkins: Nature **373** (1995) 595.

10) V. N. Ingal and E. A. Beliaevskaya: J. Phys. D **28** (1995) 2314.
11) D. Chapman, W. Thomlinson, R. E. Johnston, D. Washburn, E. Pisano, N. Gmür, Z. Zhong, R. Menk, F. Arfelli and D. Sayers: Phys. Med. Biol. **42** (1997) 2015.
12) A. Snigirev, I. Snigireva, V. Kohn, S. Kuznetsov and I. Schelokov: Rev. Sci. Instrum. **66** (1995) 5486.
13) K. A. Nugent, T. E. Gureyev, D. F. Cookson, D. Paganin and Z. Barnea: Phys. Rev. Lett. **77** (1996) 2961.
14) S. W. Wilkins, T. E. Gureyev, D. Gao, A. Pogany and A. W. Stevenson: Nature **384** (1996) 335.
15) P. Cloetens, W. Ludwig, J. Baruchel, D. Van Dyck, J. Van Landuyt, J. P. Guigay and M. Schlenker: Appl. Phys. Lett. **75** (1999) 2912.
16) F. A. Dilmanian, Z. Zhong, B. Ren, X. Y. Wu, L. D. Chapman, I. Orion and W. C. Thomlinson: Phys. Med. Biol. **45** (2000) 933.
17) I. Koyama, Y. Hamaishi and A. Momose: AIP Conf. Proc. **705** (2004) 1283.
18) A. Maksimenko, M. Ando, H. Sugiyama and T. Yuasa: Appl. Phys. Lett. **86** (2005) 124105.
19) I. Koyama, A. Momose, J. Wu, Thet Thet Lwin and T. Takeda: Jpn. J. Appl. Phys. **44** (2005) 8219.
20) Konica Minolta Technol. Rep. **2** (2005) 30 [in Japanese].
21) C. David, B. Nöhammer, H. H. Solak and E. Ziegler: Appl. Phys. Lett. **81** (2002) 3287.
22) A. Momose, S. Kawamoto, I. Koyama, Y. Hamaishi, K. Takai and Y. Suzuki: Jpn. J. Appl. Phys. **42** (2003) L866.
23) A. Momose, S. Kawamoto, I. Koyama and Y. Suzuki: Proc. SPIE **5535** (2004) 352.
24) T. Weitkamp, B. Nöhammer, A. Diaz, C. David and E. Ziegler: Appl. Phys. Lett. **86** (2005) 054101.
25) T. Weitkamp, A. Daiz, C. David, F. Pfeiffer, M. Stampanoni, P. Cloetens and E. Ziegler: Opt. Express **13** (2005) 6296.
26) S. Yokozeki and T. Suzuki: Appl. Opt. **10** (1971) 1575.
27) A. W. Lohmann and D. E. Silva: Opt. Commun. **2** (1971) 413.
28) A. Momose and S. Kawamoto: Jpn. J. Appl. Phys. **45** (2006) 314.
29) M. Matsumoto, K. Takiguchi, M. Tanaka, Y. Hunabiki, H. Takeda, A. Momose, Y. Utsumi and T Hattori: High Aspect Ratio Micro Structure Technology Workshop, 2005, p. 22.
30) P. Cloetens, J. P. Guigay, C. De Martino, J. Baruchel and M. Schlenker: Opt. Lett. **22** (1997) 1059.
31) H. F. Talbot: Philos. Mag. **9** (1836) 401.
32) J. P. Guigay: Opt. Acta **18** (1971) 677.
33) M. Born and E. Wolf: *Principle of Optics* (Pergamon Press, Oxford, 1980) p. 508.
34) J. H. Bruning, D. R. Herriott, J. E. Gallagher, D. P. Rosenfeld, A. D. White and D. J. Brangaccio: Appl. Opt. **13** (1974) 2693.
35) K. A. Stetson and W. R. Brohinsky: Appl. Opt. **24** (1985) 3631.
36) J. M. Huntley: Appl. Opt. **28** (1989) 3268.
37) G. W. Faris and R. L. Byer: Appl. Opt. **27** (1988) 5202.
38) A. Momose, T. Takeda, Y. Itai and K. Hirano: Nat. Med. **2** (1996) 473.
39) A. Momose, T. Takeda and Y. Itai: unpublished.
40) K. Patorski: *Progress in Optics* (Elsevier, Amsterdam, 1989) Vol. 27.
41) W. Yashiro and A. Momose: in preparation.